Dispersions of 1,3,4-Oxadiazole-Linked Conjugated Microporous Polymers with Carbon Nanotubes as a High-Performance Electrode for Supercapacitors

Mohamed Gamal Mohamed,*[,#] Maha Mohamed Samy,[#] Tharwat Hassan Mansoure, Santosh U. Sharma, Ming-Shiuan Tsai, Jung-Hui Chen, Jyh-Tsung Lee, and Shiao-Wei Kuo*

ACCESS | 📊 Metrics & More | 📖 Article Recommendations | 🆘 Supporting Information

Py-OXD-CMP → (π−π stacking) → Py-OXD-CMP/SWCNT

❖ Surface area: 298 m²/g
❖ Higher T_d: 420 °C
❖ Higher char yield: 61 wt%
❖ Specific capacitance: 504 F g⁻¹

ABSTRACT: In this study, we used classical and simple Sonogashira couplings to construct three 1,3,4-oxadiazole-linked conjugated microporous polymers (OXD-CMPs) through the reaction of 2,5-bis(4-bromophenyl)-1,3,4-oxadiazole (OXD-Br$_2$) as a common partner with the structurally diverse units of ethynyl triphenylamine, tetraphenylethene, and pyrene, respectively. We used several methods, both spectroscopic and microscopic, to characterize the three OXD-CMPs. Each OXD-CMP displayed a high thermal stability. The Py-OXD-CMP possessed pores having sizes in the range 1.20−2.25 nm and a high surface area (298 m^2 g^{-1}). These OXD-CMPs interacted with singled-walled carbon nanotubes (CNTs), stabilized through noncovalent π−π interactions, to afford OXD-CMP/CNT composites that were suitable for supercapacitor devices. Among our OXD-CMP/CNT composites, the Py-OXD-CMP/CNT composite offered a specific capacitance of 504 F g^{-1} and a superior capacitance retention (91.1%) over 2000 cycles.

KEYWORDS: 1,3,4-oxadiazole, conjugated microporous polymers, Sonogashira coupling, carbon nanotubes, electrochemical performance
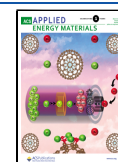
INTRODUCTION

Supercapacitors are attractive energy storage systems for electronic devices (e.g., electronic vehicles, digital communications, and portable and wearable electronics) because of their high charge/discharge rates, outstanding power densities, long cycle lives, equilibrium rate performance, superior cycle efficiencies, and environmentally friendliness.[1−8] Depending on their storage mechanisms, there are two types of supercapacitors [pseudocapacitors or electric double-layer capacitors (EDLCs)]; pseudocapacitors store energy electrochemically (faradic reactions), while EDLCs store energy electrostatically between the electrolyte solution and the electrode surface.[9,10] A variety of organic and inorganic substances have been used as the electrodes for supercapacitors, including carbon nanotubes (CNTs), activated carbons, metal oxides, sulfides, hydroxides, and composites.[11−15] Lately, porous organic materials [covalent organic frameworks, covalent triazine framework, and conjugated microporous polymers (CMPs)] have been employed as

EDLC electrodes on account of their low cost, chemical stability, flexibility, and availability; these substances have a role in determining the efficiency of the supercapacitor.[16−29] CMPs are novel polymeric materials that have attracted much attention for their entirely π-conjugated skeletons, ease of preparation, excellent rigidity, well-defined porosities, high surface areas, great thermal stabilities, and good optoelectronic characteristics.[30−32] Various chemical and electrochemical methods have been developed for the preparation of CMPs from suitable building blocks by linking them through a range of coupling
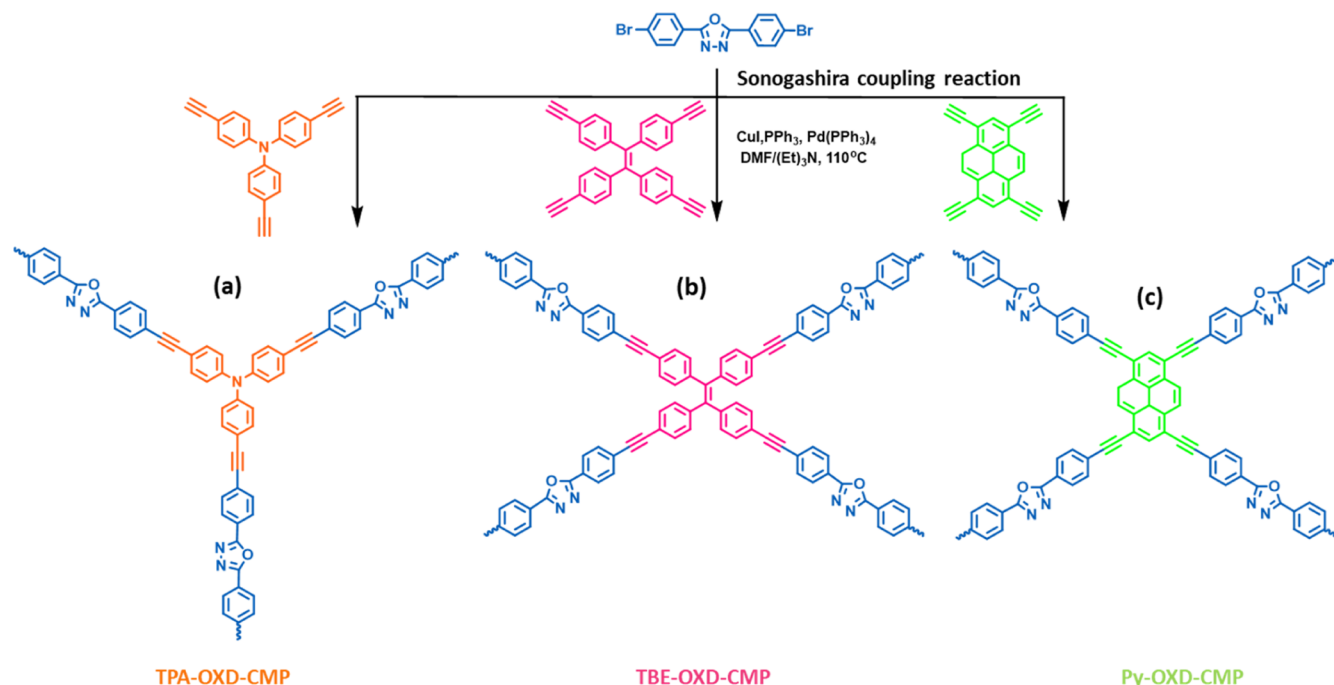
Scheme 1. Preparation of (a) TPA-OXD, (b) TPE-OXD, and (c) Py-OXD-CMPs

polymerizations.[33,34] The resulting CMPs have been employed in such fields as catalysis, hydrogen evolution, sensors, dye adsorption, gas storage, photocatalysis, energy conversion, and energy storage.[35−43] Because of the relatively low conductivities of CMPs, pyrolysis methods have often been used to improve their capacitance when applied as electrodes for supercapacitors.[44−47] Nevertheless, the products of pyrolysis do not always possess improved capacitance or cycling stability. For example, Feng et al. found that polyarene-CMPs had a capacitance of only 110 F g^{-1} after pyrolysis process[48] and Samy et al. reported that Py-FFC-CMP/poly(β-CD-BZ) inclusion complexes materials, displayed the capacitance of only 46 F g^{-1} at 0.5 Ag^{-1} after curing the sample at 300 °C.[49] An alternative and more efficient means of promoting the conductivity of CMPs is to incorporate them with conducting carbon materials (e.g., graphene and CNTs), leading to an enhanced electrochemical performance.[50−53] Because of their nanostructures, remarkable mechanical characteristics, and exceptional electrical and thermal conductivities, CNTs have found applications in, for example, supercapacitors, fuel cells, electronics, sensors, solar cells, and conductive films.[54−56] High-conductivity CMPs incorporating active CNTs can also maintain high stability during the charge/discharge step, resulting in supercapacitors displaying a more efficient performance. For instance, Duan et al. revealed a CoPc-CMP/CNT possessing the capacitance of 365 F g^{-1}.[57] Lin and co-workers prepared a CNT@Mn-MOF composite having the capacitance of 203 F g^{-1}.[58] We constructed a TBN-Py-CMP/CNT nanocomposite material with a high capacitance value (430 F g^{-1}).[59]

1,3,4-Oxadiazole is a heterocyclic molecule having a five-membered ring. Because of their good luminescent and thermal characteristics, materials containing oxadiazole units have been used in, for example, coordination polymers, metal ion sensors, liquid crystals, and organic light-emitting diodes.[60−62] A few research groups have synthesized CMPs containing OXD moieties as electron-withdrawing groups. For example, Liu et
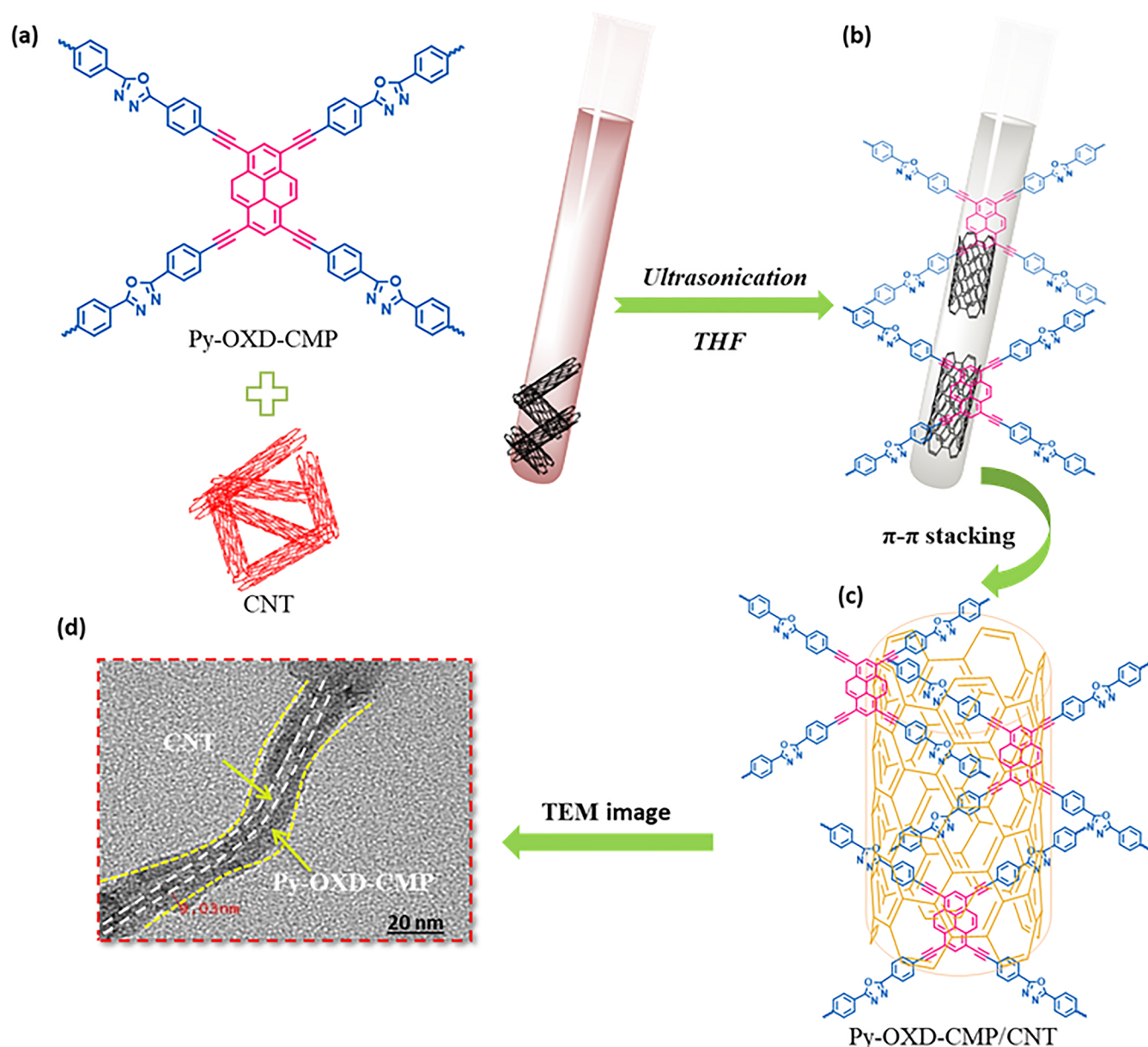
al. reported a TPA-OXD material that provided high CO production from CO$_2$ with high selectivity;[63] the Yi group prepared two CMP materials [Ph(ThXOD)$_3$-CMP and Ph-(PhXOD)$_3$] through Suzuki coupling for the degradation of methylene blue and rhodamine B under visible light.[64] However, this present study is the first to employ OXD-CMPs and OXD-CMP/CNT materials for energy storage. We found that the integration of CNTs with OXD-linked CMPs, stabilized through noncovalent bonding interactions, afforded OXD-CMP/CNT composites possessing greatly enhanced capacitance and cycling stability when employed as electrodes for supercapacitors. For this study, we synthesized three different OXD-CMPs through simple Sonogashira couplings denoted as TPA-OXD-CMP, Py-OXD-CMP, and TPE-OXD-CMP of OXD-Br$_2$ as a common monomer with ethynyl derivatives of triphenylamine, tetraphenylethene, and pyrene, respectively (Scheme 1). We used various spectroscopic and microscopic methods to characterize our prepared OXD-CMPs. In addition, we used transmission electron microscopy (TEM) to investigate the formation of corresponding OXD-CMP/CNT composites featuring the dispersion of the CNTs throughout the OXD-CMP matrices.

■ **EXPERIMENTAL SECTION**

Materials. Copper iodide (CuI), Pd(PPh$_3$)$_4$, and triphenylphosphine (PPh$_3$) were obtained from Sigma-Aldrich. Hydrazine hydrate solution (NH$_2$NH$_2$·H$_2$O), triethylamine (Et$_3$N), dichloromethane (CH$_2$Cl$_2$, DCM), and N,N-dimethylformamide (DMF) were purchased from Acros. TPE-T and Py-T were synthesized using reported procedures previously.[59,65]

Synthesis of Tris(4-((trimethylsilyl)ethynyl)phenyl)amine. Pd(PPh$_3$)$_4$ (0.150 mmol), PPh$_3$ (0.470 mmol), CuI (0.310 mmol), and TPA-Br$_3$ (2.07 mmol) in THF (50 mL). Trimethylsilyl acetylene (1.42 g, 15.5 mmol) was added, and mixtures were refluxed for 3 days. After cooling, the contents inside the flask were endowed for cooling and then filtered off, extracted with DCM (50 mL), and then, the solvent was evaporated and the pure tris(4-((trimethylsilyl)ethynyl)-phenyl)amine (TPA-TMS) as a yellow solid was obtained after running

Scheme 2. (a,b) Blending of the Py-OXD-CMP and CNT Nanocomposite in THF Solution with the Ultrasonication Process; (c) Formation of the Py-OXD-CMP/CNT Nanocomposite; (d) Dispersion of CNT Throughout the Py-OXD-CMP Matrix (TEM Image)

column chromatography (Scheme S1). Fourier transform infrared (FTIR) (Figure S1): 3035, 2109 (C≡C stretching). ^{1}H NMR (Figure S2): 7.34 (s, 6H), 6.97 (s, 6H), 0.257 (s, 27H, CH$_3$) ppm. ^{13}C NMR (Figure S2): 148.14, 134.03, 124.83, 118.49, 105.83, 93.83, 0.09 ppm.

Synthesis of Tris(4-ethynylphenyl)amine. TPA-TMS (0.520 g, 0.970 mmol) and K$_2$CO$_3$ (1.00 g, 7.24 mmol) were stirred in MeOH (25 mL) at 27 °C for 1 d. The solvent was evaporated and added H$_2$O (100 mL) to give tris(4-ethynylphenyl)amine (TPA-T) (0.45 g, 87%, Scheme S1). FTIR (Figure S1, cm^{-1}): 3276 (≡C–H), 2109 (C≡C stretching), cm^{-1}. ^{1}H NMR (Figure S2): 7.39 (s, 6H), 7.03 (s, 6H), 3.04 (s, 3H) ppm. ^{13}C NMR (Figure S2): 148.48, 134.03, 124.15, 117.8, 83.28 ppm.

Synthesis of N,N′-Bis(4-bromobenzoyl)hydrazine. In an ice bath, Et$_3$N (3.00 mL, 21.6 mmol) and 4-bromobenzoyl bromide (2.40 g, 9.09 mmol) in CHCl$_3$ (50 mL) were added. Then, NH$_2$NH$_2$·H$_2$O (0.24 mL) was added and allowed for stirring over 12 h. The resulting white solid was washed thoroughly with NaHCO$_3$ solution (10%) and water, and dried, and then used directly in the next step (Scheme S2). FTIR (Figure S3): 3190 (NH), 3032, 1650 (C=O) cm^{-1}. ^{1}H NMR

(Figure S4): 10.67 (NH), 7.74 (d, 4H), 7.85 (d, 4H) ppm, ^{13}C NMR (Figure S4): 166.21, 132.51, 129.65, 127.21 ppm.

Synthesis of OXD-Br$_2$. A mixture of N,N′-bis(4-bromobenzoyl)-hydrazine (1.42 g, 3.56 mmol) and POCl$_3$ (30 mL) was heated at 90 °C for 8 h. The mixture was poured into cold water to produce white needles. The white product was washed with water and cold EtOH to afford OXD-Br$_2$ (85%, Scheme S2). FTIR (Figure S3): 3086, 1600, 742 cm^{-1}. ^{1}H NMR (Figure S4): 8.07 (d, 4H), 7.85 (d, 4H) ppm. ^{13}C NMR (Figure S4): 164.11, 133.52, 128.98, 126.11, 122.66 ppm.

Preparation of TPA-OXD-CMP, TPE-OXD-CMP, and Py-OXD-CMP. OXD-Br$_2$ (0.65 mmol) and TPA-T (0.31 mmol), TPE-T (0.23 mmol), or Py-T (0.34 mmol) were mixed in DMF and Et$_3$N. CuI (0.068 mmol), PPh$_3$ (0.030 mmol), and Pd catalyst (0.031 mmol) were added, and then, the mixture was degassed three times using a freezing pump. The tube was heated at 115 °C for 3 days. The obtained CMP was washed with THF, MeOH, and cold acetone and then dried at 90 °C for 18 h to afford TPA-OXD-CMP (yellow powder, 81%), TPE-OXD-CMP (orange powder, 73%), or Py-OXD-CMP (dark red powder, 75%) (Scheme 1).
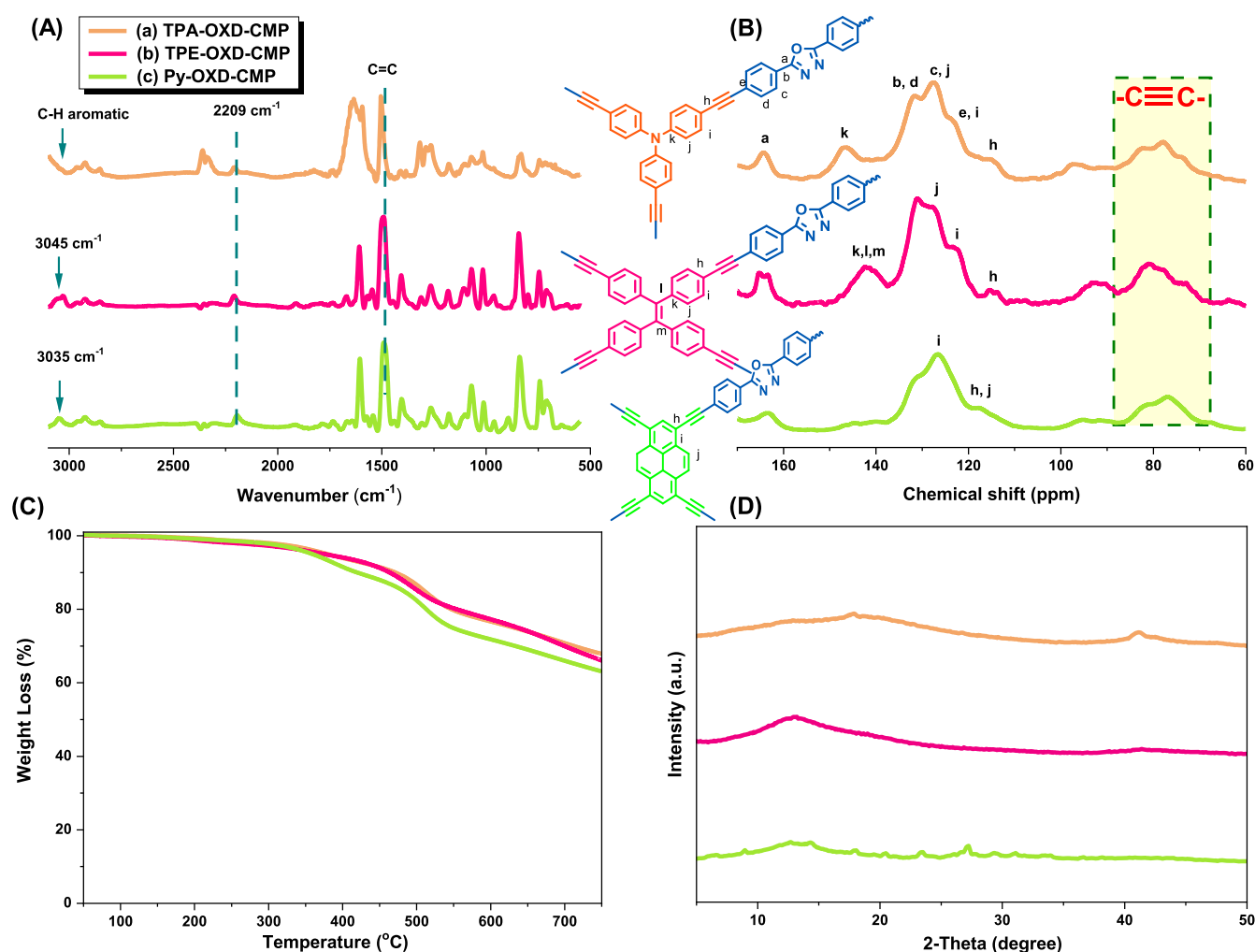
Figure 1. (A) FTIR, (B) ^{13}C NMR, (C) TGA, and (D) XRD profiles of (a) TPA-OXD, (b) TPE-OXD, and (c) Py-OXD-CMPs.
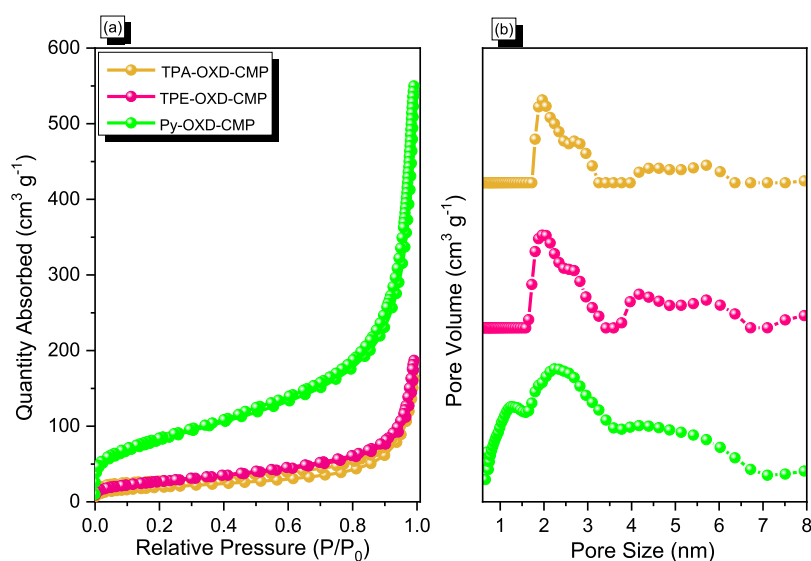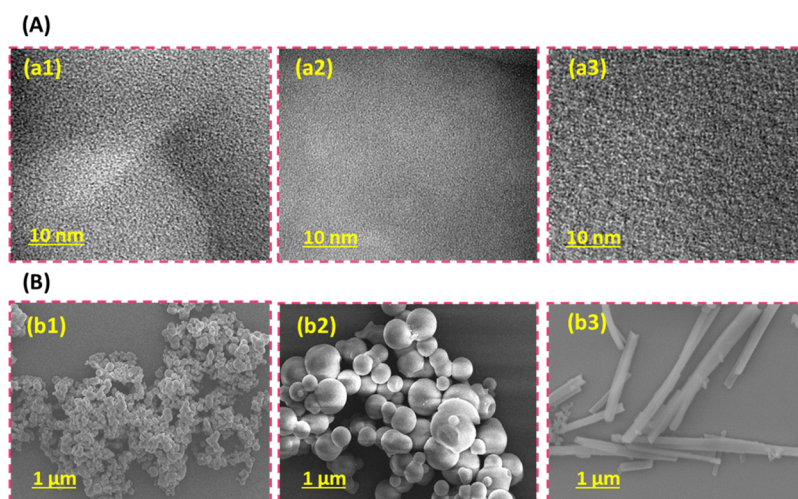

Figure 2. (a) N$_2$ sorption and (b) PSD curves of TPA-OXD, TPE-OXD, and Py-OXD-CMPs.

Preparation of OXD-CMP/CNT Nanocomposites. OXD-CMP (2 wt %) and CNTs (2 wt %) were mixed well in THF with stirring for 1 day. The THF was evaporated, and the residue heated in an oven for 24 h to afford an OXD-CMP/CNT nanocomposite, which was characterized using TEM (Scheme 2).

RESULTS AND DISCUSSION

Synthesis and Characterization of OXD-CMPs. We prepared TPA-OXD, TPE-OXD, and Py-OXD-CMPs through Sonogashira couplings of OXD-Br$_2$ with TPA-T, TPE-T, and
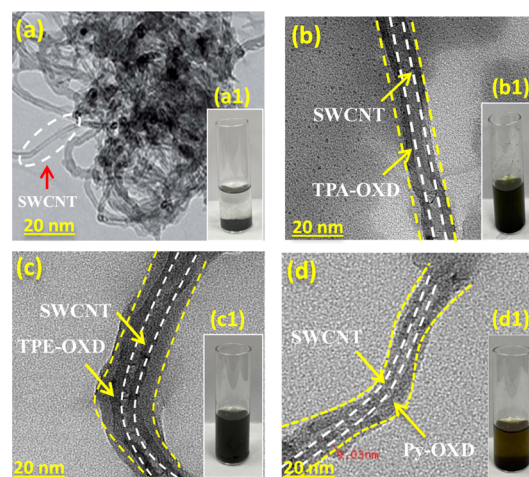
Figure 3. (A) TEM and (B) SEM images of (a1,b1) TPA-OXD, (a2,b2) TPE-OXD, and (a3,b3) Py-OXD-CMPs.

Py-T, respectively, using anhydrous DMF and Et$_3$N as solvents and Pd as the catalyst (Scheme 1). We characterized these three OXD-CMPs using various methods. The FTIR spectra of the OXD-CMPs all featured absorption peaks near 2209 cm^{-1} representing symmetrical C≡C bonds, confirming the existence of alkyne linkages in their structures. In addition, a signal appeared near 3045−3035 cm^{-1} for vibrations of the aromatic C−H units [Figure 1A]. The solid-state NMR spectra of the three OXD-CMPs had signals at 81 and 78.5 ppm, representing C≡C carbon nuclei in the OXD-CMP structures. In addition, a broad signal appeared in the spectrum of each of these OXD-CMPs at 164 ppm, representing the O−C−N carbon nuclei of the OXD rings, as well as signals in the range 116−146 ppm for the aromatic carbon nuclei. A distinct signal appeared at 142 ppm in the spectrum of TPE-OXD-CMP [Figure 1B], corresponding to ethylene groups of the TPE moieties. We used thermogravimetric analysis (TGA) to examine the thermal stabilities of these three OXD-CMPs. The weights of TPA-OXD-CMP, TPE-OXD-CMP, and Py-OXD-CMP remained constant up to 400 °C, with subsequent 10 wt % weight losses of 471, 464, and 420 °C, respectively; their char yields at 800 °C were 66, 62, and 61 wt %, respectively [Figure 1C and Table S1]. The X-ray diffraction (XRD) pattern of each of the three OXD-CMPs featured a broad band at a value of 2θ of approximately 13°; the absence of any ordered diffraction peaks illustrated their amorphous nature [Figure 1D].

We performed N$_2$ sorption analyses at 77 K to evaluate the porous characteristics of the OXD-CMPs. Acoording to the N$_2$ isotherms, TPA-OXD-CMP, TPE-OXD-CMP, and Py-OXD-CMP provided IUPAC type-II isotherms with surface areas of 76, 96, and 298 m^2 g^{-1}, respectively [Figure 2a and Table S1]. The pore size distributions of the OXD-CMPs, assessed using nonlocal density functional theory, were 1.96 and 2.76 nm for TPA-OXD-CMP, 1.96 and 2.63 nm for TPE-OXD-CMP, and 1.20 and 2.25 nm for Py-OXD-CMP. Thus, the surfaces of the OXD-CMP materials featured interfacial micropores [Figure 2b and Table S1].

TEM images for three OXD-CMPs verified their microporous morphologies (pore diameters: <50 nm) [Figure 3A(a1−a3)]. The surface morphologies of the OXD-CMPs displayed an aggregated sphere morphology for TPA-OXD-CMP, sphere structure for TPE-OXD-CMP, and nanorod structure for the Py-OXD-CMP sample based on SEM images [Figure 3B(b1−b3)].
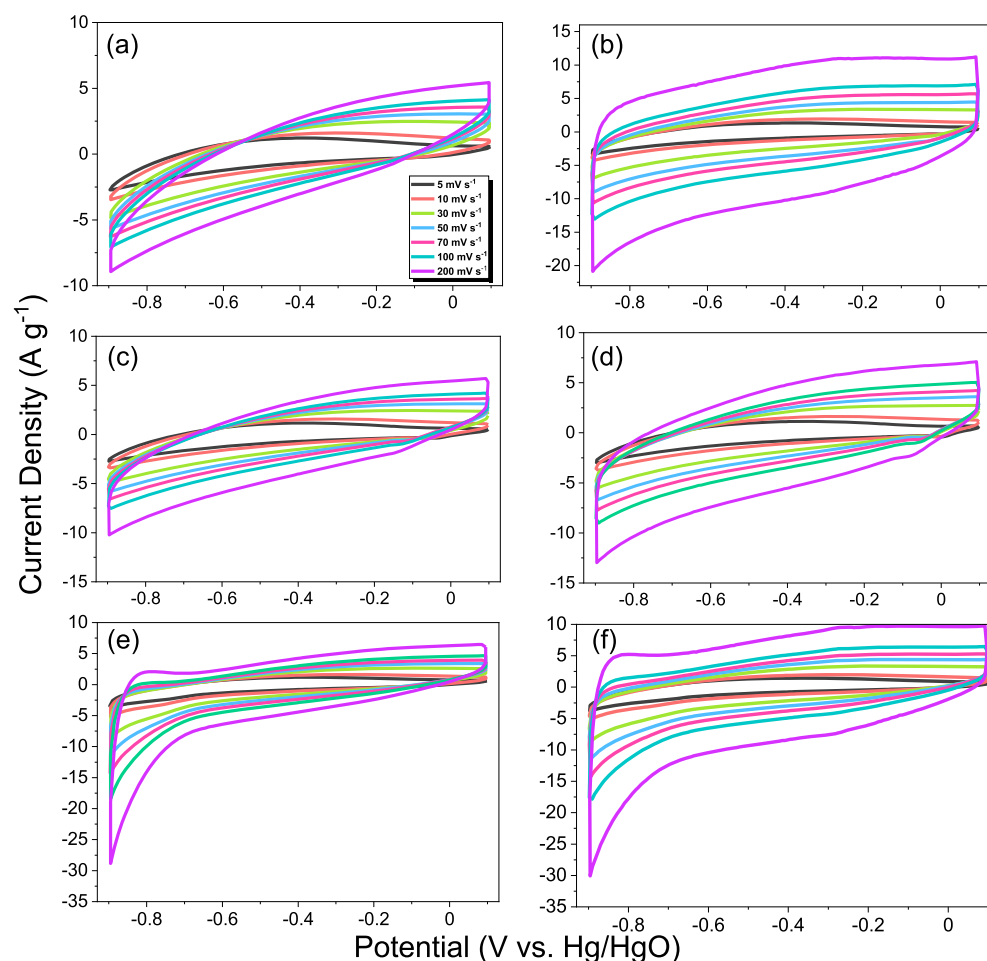
Figure 4 displays TEM photos of the singled-walled CNT (SWCNT) and the OXD-CMP/CNT nanocomposites (TPA-

Figure 4. (a−d) TEM photos of the (a) pure CNTs, (b) TPA-OXD, (c) TPE-OXD, and (d) Py-OXD-CMPs/CNT nanocomposites. (a1−d1) Photographs of the (a1) CNTs, (b1) TPA-OXD, (c1) TPE-OXD, and (d1) Py-OXD-CMPs/CNT nanocomposites in THF.

CMP/CNT, TPE-CMP/CNT, and Py-CMP/CNT). As revealed in the photograph in Figure 4(a1), the CNTs aggregated when added in THF, as confirmed using TEM [Figure 3a]. Gratifyingly, when the OXD-CMPs were added to the aggregated CNTs, the OXD-CMPs/CNT complexes dissolved [Figure 4b1,c1,d1] as a result of π-stacking interactions among the CNT nanoparticles and the OXD-CMPs. The TEM images in Figure 4b−d reveal the remarkable dispersions of the CNTs throughout the matrices of the OXD-CMPs.[56,59,66−68]

Electrochemical Performance of OXD-CMP and Their CNT Nanocomposites. We performed CV and GCD analyses in the three-electrode system to test the electrochemical activity of the OXD-CMP materials and their blends with the SWCNTs in 1 M KOH as the aqueous electrolyte. Figure 5a−f presents the CV curves of the OXD-CMPs and the OXD-CMP/CNT nanocomposites, measured at various scan rates from 5 to 200 mV s^{-1}. The CV curves of all of the samples were rectangular in
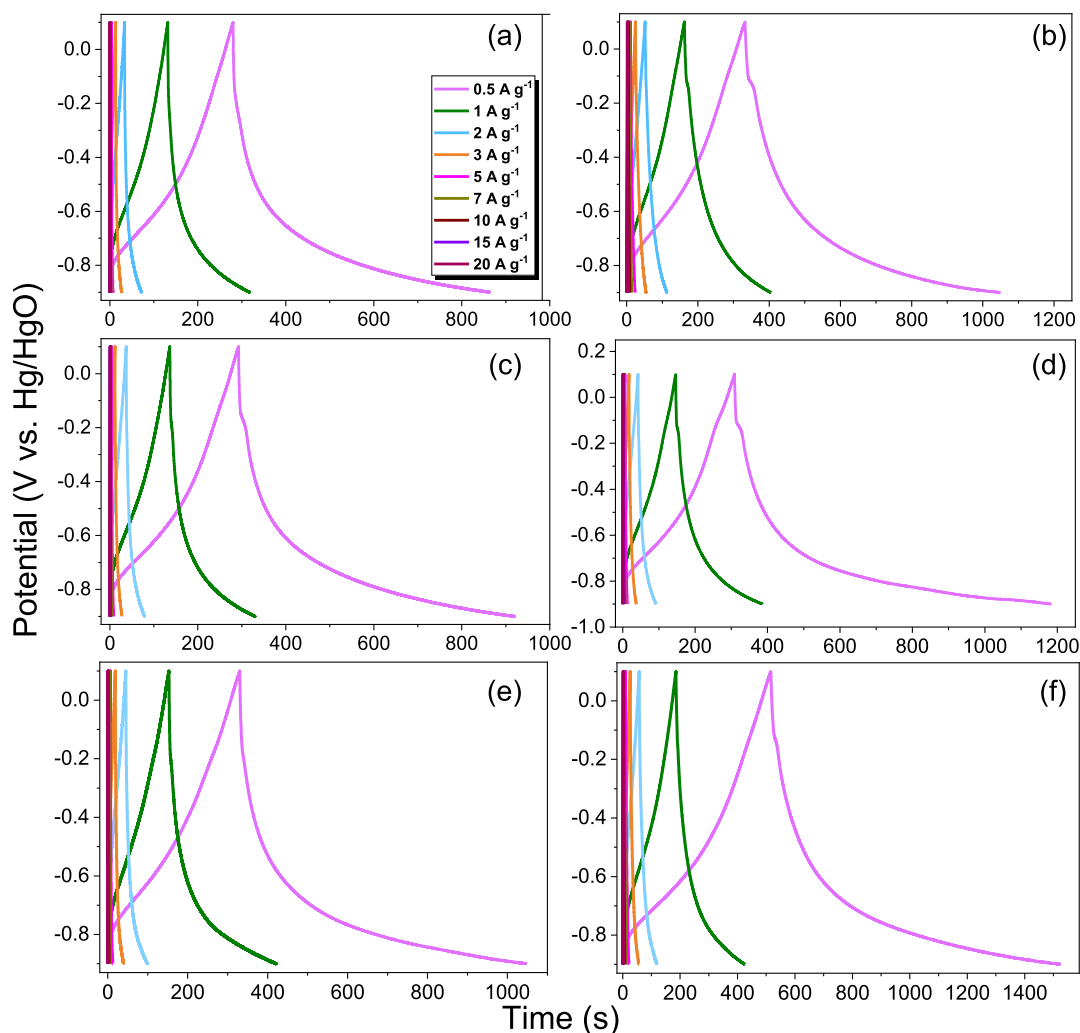
Figure 5. CV patterns of (a) TPA-OXD-CMP, (b) the TPA-OXD-CMP/CNT nanocomposite, (c) TPE-OXD-CMP, (d) the TPE-OXD-CMP/CNT nanocomposite, (e) Py-OXD-CMP, and (f) the Py-OXD-CMP/CNT nanocomposite.

shape with the appearance of humps, even when recorded at 200 mV s^{-1}, originated from their EDLC with minor pseudocapacitance.[57,59,69] The pseudocapacitance arose from the presence of heteroatoms (i.e., N and O atoms).[57,59,69] The current density increased upon increasing the scan rate, indicating facile kinetics and good rate capability.[57,59,69] Figure 5b,d,f reveals that the introduction of the CNTs into the OXD-CMPs increased the CV integrated areas, relative to those of the pure OXD-CMPs, suggesting the enhanced specific capacitance of the OXD-CMP/CNT nanocomposites.

Figure 6a−f shows the GCD patterns of the OXD-CMPs and the OXD-CMP/CNT nanocomposites at different current densities. The GCD curves of all of the pure and CNT-supported OXD-CMPs were triangular in shape at all of the current densities, but featuring slight bends, suggesting both pseudocapacity and EDLC features.[57,59,69] In addition, the OXD-CMP/CNT nanocomposites showed longer discharging times than those of the pure OXD-CMPs. These results confirmed that the CNTs enhanced the capacitance performance of the OXD-CMPs. Furthermore, the higher Coulombic efficiencies of our OXD-CMPs and their nanocomposites due to the fast intercalation and surface diffusion of the electrolyte ions during the charging process and slow deintercalation of the electrolyte ions during the discharging process which suggests OXD-CMP materials may be utilized as a promising hybrid battery-type supercapacitor.[6]

Figure 7 presents the specific capacitances of all of the OXD-CMP-based samples, determined from their GCD curves using eq S1. At a current density of 0.5 A g^{-1}, the capacitance of the Py-OXD-CMP/CNT nanocomposite (504 F g^{-1}) was excellent and much higher than those of the other OXD-CMP-based samples (Py-OXD-CMP: 359 F g^{-1}; TPE-OXD-CMP: 313 F g^{-1}; TPE-OXD-CMP/CNT nanocomposite: 437 F g^{-1}; TPA-OXD-CMP: 292 F g^{-1}; and TPA-OXD-CMP/CNT nanocomposite: 360 F g^{-1}) [Figure 7a−c]. We attribute this behavior to the higher surface area (298 m^2 g^{-1}), the existence of micro- and mesoporosity (pore sizes: 1.96 and 2.76 nm), and the presence of various types of N and O heteroatoms, all of which ensured greater accessibility of the electrolyte to the electrode surface.[57,59,69,70] Upon increasing the current density, the capacitances of all of the OXD-CMP-based samples decreased due to the difficult ion adsorption and diffusion inside the smallest pores at higher current densities.[57,59,69] Recently, our group prepared three types of TBN-CMPs based on tetrabenzonaphthalene (TBN), carbazole (Car), TPE, and Py units and then blended them with CNTs to improve their conductivity.[59] Electrochemical analysis revealed that our TBN-Py-CMP/CNT sample had an excellent capacitance of 430 F g^{-1} compared with other TBN-CMPs/CNT precursors due to the strong interaction between CNTs and TBN-Py-CMP via π−π stacking.[59] In addition, Mei et al. prepared copper porphyrin-linked CMP (CuTAPP-CMP) CNTs;[69] electrochemical testing revealed that the CuTAPP-CMP/CNT nanocomposite had a
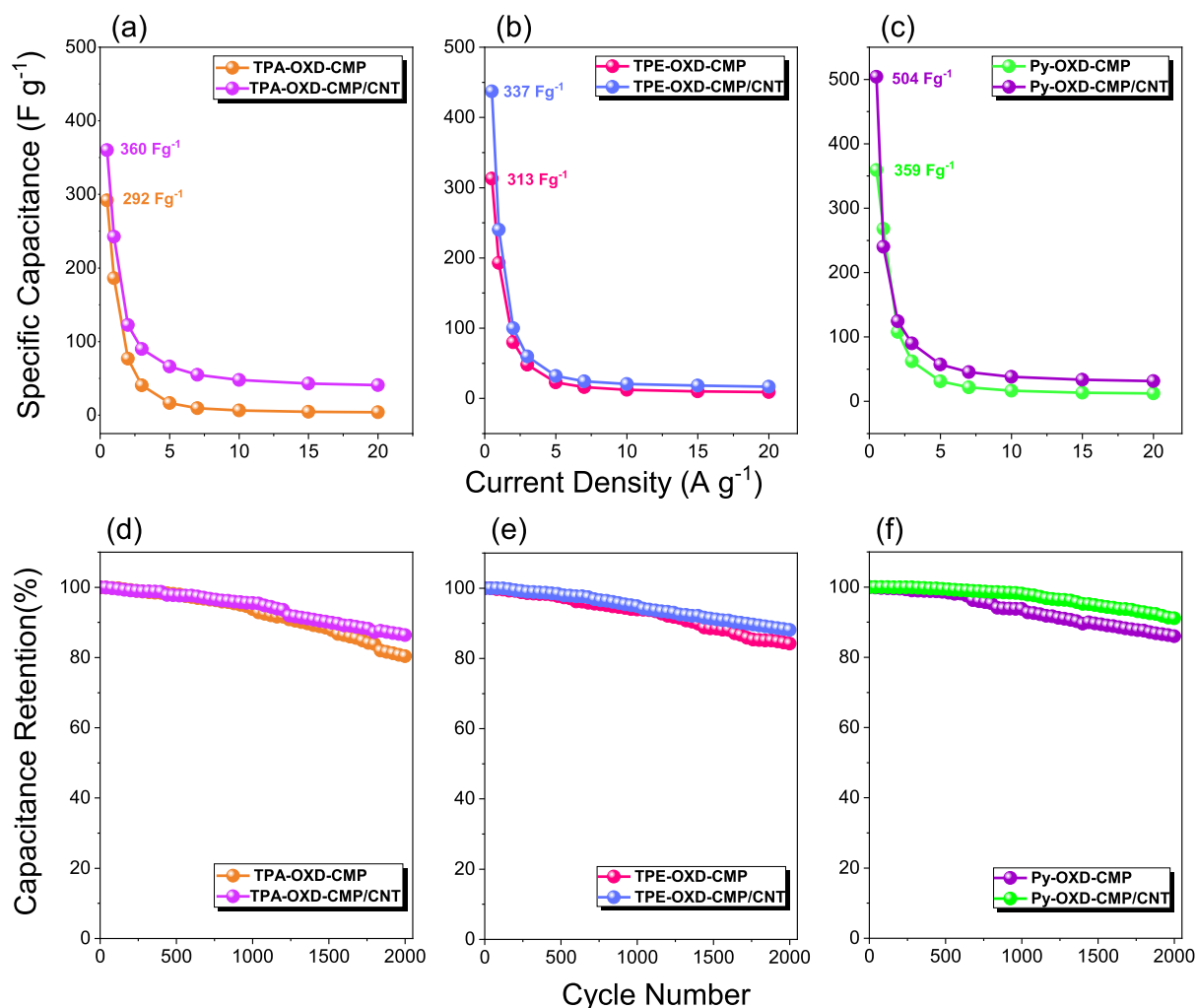
Figure 6. GCD curves of (a) TPA-OXD-CMP, (b) the TPA-OXD CMP/CNT nanocomposite, (c) TPE-OXD-CMP, (d) the TPE-OXD-CMP/CNT nanocomposite, (e) Py-OXD-CMP, and (f) the Py-OXD-CMP/CNT nanocomposite.

specific capacitance of 207.8 F g^{-1} with an excellent long cycle performance.

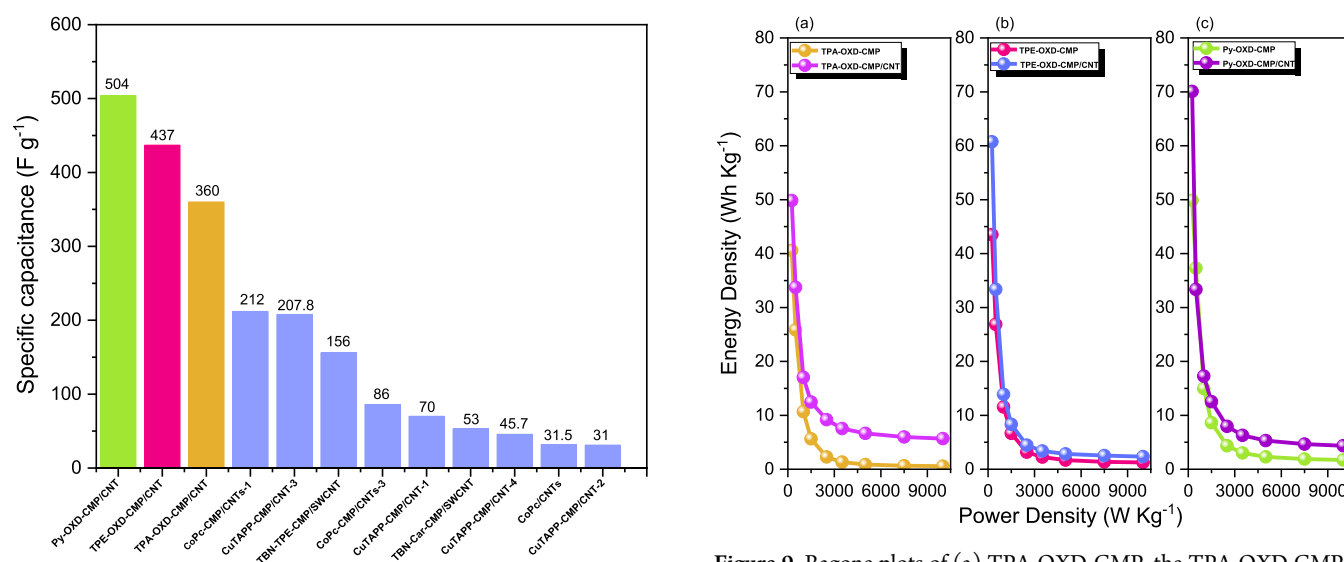Accordingly, we examined the durability of our samples through GCD measurements over 2000 cycles at a current density of 10 A g^{-1}. The TPA-OXD-CMP, TPE-OXD-CMP, Py-OXD-CMP, TPA-OXD-CMP/CNT, TPE-OXD-CMP/CNT, and Py-OXD-CMP/CNT displayed good cycling stability (Figure 7d−f), with capacitance retentions of 86.1, 84.2, 80.4, 91.1, 88.1, and 86.4%, respectively, of their original capacitances after 2000 cycles; thus, the cycling stability of the OXD-CMPs improved after their blending with the CNTs. Furthermore, Figure 8 and Table S2 presented the excellent energy storage performance of the OXD-CMPs/CNT precursor compared with other CMP/CNT materials.[57,59,69]

We calculated the energy and power densities using eqs S2 and S3, respectively, to construct a Ragone plot [Figure 9a−c], which revealed that the energy density of the Py-OXD-CMP/CNT nanocomposite (70.1 W h kg^{-1}) was higher than those of our other tested OXD-CMP-based samples (Py-OXD: 50 W h kg^{-1}; TPE-OXD: 43.5 W h kg^{-1}; TPE-OXD/CNT nanocomposite: 60.7 W h kg^{-1}; TPA-OXD: 40.6 W h kg^{-1}; and TPA-OXD/CNT nanocomposite: 49.9 W h kg^{-1}) at a power density of 250 W kg^{-1}.

To further explore the practical application prospect of OXD-CMPs/CNT nanocomposites as supercapacitor, the assembled symmetric supercapacitor was tested in a two-electrode system. CV and GCD curves of OXD-CMPs/CNT nanocomposites were recorded within the potential window of 0.10 to −0.90 V at sweep rates (5−200 mV s^{-1}) and current densities (0.50−20 A g^{-1}), respectively, and presented in Figure 10. As shown in Figure 10a−c, the CVs at different scan rates have rectangular shape even at a high scan rate (200 mV s^{-1}), suggesting an EDLC behavior. The humps present in the CV profiles were due to the pseudocapacitance behavior, arising from the presence of heteroatoms (i.e., N and O atoms). In addition, as the scan rate increases, the corresponding current at the same potential also increases, indicating that the symmetric capacitor has good reversibility. Moreover, the GCD curves of the OXD-CMPs/CNT symmetric cell (Figure 10e,f) are triangular in shape, indicating that they have a good capacitance performance. At a current density of 0.5 A g^{-1}, the capacitance of the Py-OXD-CMP/CNT nanocomposite (409.4 F g^{-1}) was excellent and higher than those of the other OXD-CMPs/CNT nanocomposite-based samples (TPA-OXD-CMP/CNT nanocomposite: 346 F g^{-1}; TPE-OXD-CMP/CNT nanocomposite: 299.6 F g^{-1}) [Figure S5a] in a good agreement with three electrode results. Furthermore, the durability test of the OXD-

Figure 7. (a−c) Specific capacitances and stability profiles (e−f) of the OXD-CMPs and OXD-CMPs/CNT nanocomposites.
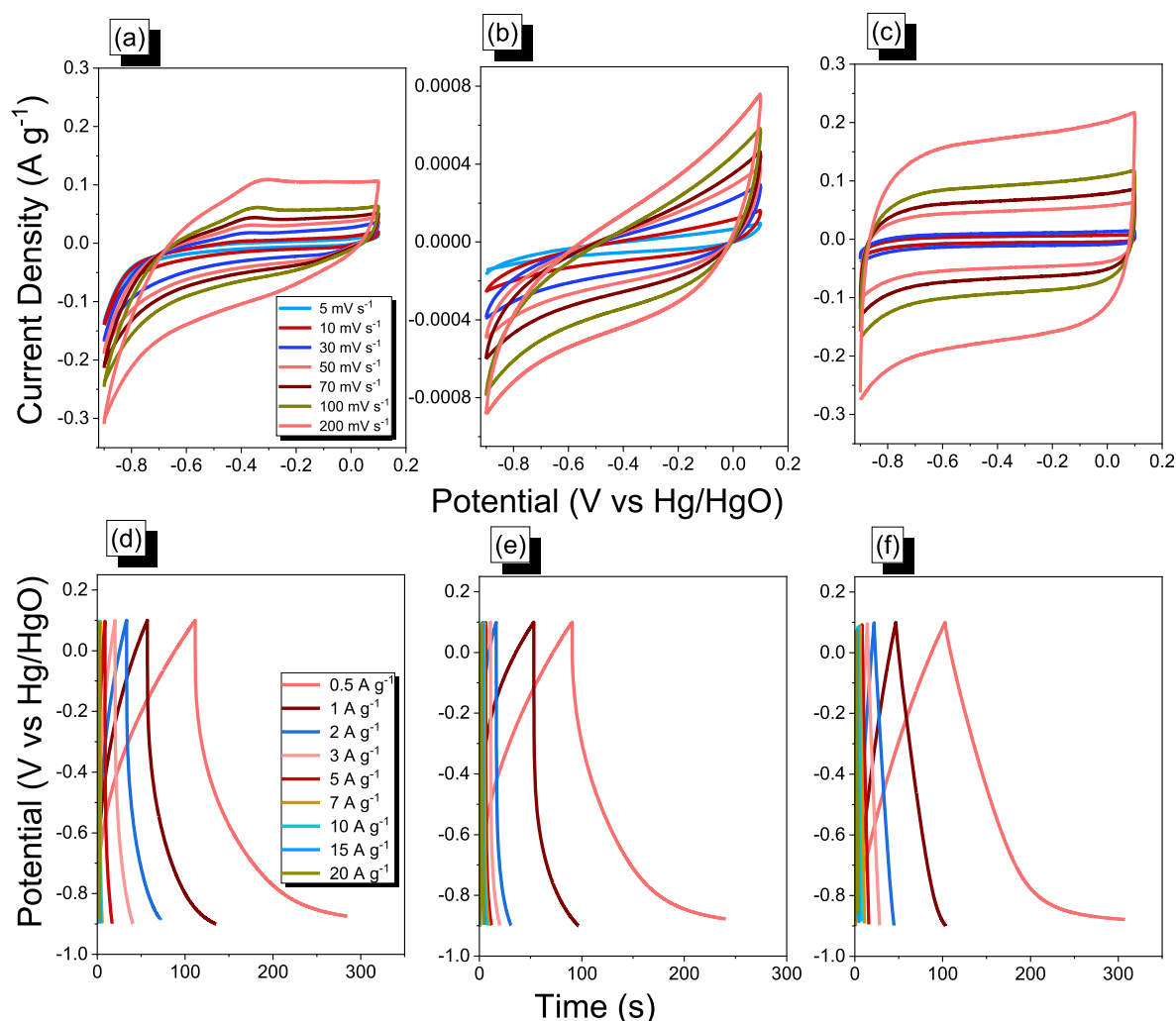

Figure 8. Specific capacitances of the OXD-CMPs/CNT nano-composites and those of other CMP/CNT materials reported previously for energy storage applications.

Figure 9. Ragone plots of (a) TPA-OXD-CMP, the TPA-OXD CMP/CNT nanocomposite, (b) TPE-OXD-CMP, the TPE-OXD-CMP/CNT nanocomposite, (c) Py-OXD-CMP, and the Py-OXD-CMP/CNT nanocomposite.

CMPs/CNT symmetric cell was performed under at a current density of 10 A g^{-1} for 1000 cycles (Figure S5b). The Py-OXD,

TPA-OXD, and TPE-OXD-CMPs/CNT displayed good cycling stability (Figure S5b), with capacitance retentions of 100, 68, and 39.4%, respectively, of their original capacitances

Figure 10. CV curves of (a) TPA-OXD, (b) TPE-OXD, and (c) Py-OXD-CMPs/CNT nanocomposites. GCD curves of (a) TPA-OXD, (b) TPE-OXD, and (c) Py-OXD-CMPs/CNT nanocomposites.

after 1000 cycles, indicating that the Py-OXD-CMP/CNT sample has a higher cycling stability performance. The Ragone plot for the OXD-CMPs/CNT symmetric cell is constructed and presented in Figure S5c. The Py-OXD-CMP/CNT nanocomposite exhibited a high energy density of 14.21 W h/kg at a power density of 250 W/kg, and when the power density increased to 10 000 W/kg, the energy density was maintained at 3.16 W h/kg compared with other OXD-CMPs/CNT and reported materials [Figure S6]. To verify the practical applications, the Py-OXD-CMP/CNT symmetric cell illuminates a red light-emitting diode, as displayed in Figure S7. Figure S8 and Table S3 display the Nyquist plots of Py-OXD, TPA-OXD, and TPE-OXD-CMPs/CNT nanocomposites. In the high-frequency region, all samples showed an obvious semi-circular feature, which represent the charge transfer resistance (R_{ct}). The Py-OXD-CMP/CNT nanocomposite has the smallest R_{ct} (7.282 Ω) compared to those of TPA-OXD-CMP/CNT (10.19 Ω) and TPE-OXD-CMP/CNT (22.96 Ω) nanocomposites, indicating that the charge transfer resistance of electrons in the electrode is the smallest.

CONCLUSIONS

We have prepared three CMPs through Sonogashira coupling of a brominated-oxadiazole (OXD-Br$_2$) building block with TPA,

TPE, and Py moieties, respectively. We then integrated these three OXD-CMPs with CNTs to produce OXD-CMP/CNT nanocomposites, which we evaluated as electrodes for super-capacitor systems. The Py-OXD-CMP/CNT electrode displayed an excellent specific capacitance (504 F g^{-1}) and cycling stability (91.1% capacitance retention). Our results suggest the promise of OXD-CMPs/CNT nanocomposites in higher-performance charge energy storage.

ASSOCIATED CONTENT

Supporting Information

The Supporting Information is available free of charge at https://pubs.acs.org/doi/10.1021/acsaem.2c00100.

Characterization part and electrochemical procedures; syntheses of TPA-TMS and TPA-T; syntheses of *N,N′*-bis(4-bromobenzoyl)hydrazine and OXD-Br$_2$; FTIR spectra of TPA-TMS and TPA-T; ^{1}H and ^{13}C NMR spectra of TPA-TMS and TPA-T; FTIR spectra of *N,N′*-bis(4-bromobenzoyl)hydrazine and OXD-Br$_2$; ^{1}H and ^{13}C NMR spectra of *N,N′*-bis(4-bromobenzoyl)-hydrazine and OXD-Br$_2$; specific capacitances and stability and Ragone profiles of TPA-OXD-CMP/CNT, TPE-OXD-CMP/CNT, and Py-OXD-CMPs/CNT; comparison of Ragone data of TPA-OXD-CMP/CNT,

TPE-OXD-CMP/CNT, and Py-OXD-CMP/CNT samples with other materials; LED glowing photo with Py-OXD-CMP/CNT; EIS spectra of the Py-OXD-CMP/CNT, TPA-OXD-CMP/CNT, and TPE-OXD-CMP/CNT; TGA and BET data of the OXD-CMPs; specific surface areas and specific capacitances of the OXD-CMP-based samples and of materials previously reported for use in supercapacitor applications; and summarized EIS data fitting of Py-OXD-CMP/CNT, TPA-OXD-CMP/CNT, and TPE-OXD-CMP/CNT (PDF)

■ AUTHOR INFORMATION

Corresponding Authors

Mohamed Gamal Mohamed − *Department of Materials and Optoelectronic Science, Center for Functional Polymers and Supramolecular Materials, National Sun Yat-Sen University, Kaohsiung 804, Taiwan; Chemistry Department, Faculty of Science, Assiut University, Assiut 71515, Egypt;* orcid.org/0000-0003-0301-8372; Email: mgamal.eldin12@yahoo.com

Shiao-Wei Kuo − *Department of Materials and Optoelectronic Science, Center for Functional Polymers and Supramolecular Materials, National Sun Yat-Sen University, Kaohsiung 804, Taiwan; Department of Medicinal and Applied Chemistry, Kaohsiung Medical University, Kaohsiung 807, Taiwan;* orcid.org/0000-0002-4306-7171; Email: kuosw@faculty.nsysu.edu.tw

Authors

Maha Mohamed Samy − *Department of Materials and Optoelectronic Science, Center for Functional Polymers and Supramolecular Materials, National Sun Yat-Sen University, Kaohsiung 804, Taiwan*

Tharwat Hassan Mansoure − *Chemistry Department, Faculty of Science, Assiut University, Assiut 71515, Egypt;* orcid.org/0000-0002-5848-0196

Santosh U. Sharma − *Department of Chemistry, National Sun Yat-Sen University, Kaohsiung 80424, Taiwan*

Ming-Shiuan Tsai − *Department of Chemistry, National Kaohsiung Normal University, Kaohsiung 802, Taiwan*

Jung-Hui Chen − *Department of Chemistry, National Kaohsiung Normal University, Kaohsiung 802, Taiwan*

Jyh-Tsung Lee − *Department of Chemistry, National Sun Yat-Sen University, Kaohsiung 80424, Taiwan;* orcid.org/0000-0002-2658-4222

Complete contact information is available at:
https://pubs.acs.org/10.1021/acsaem.2c00100

■ REFERENCES

(1) Liu, S.; Kang, L.; Zhang, J.; Jung, E.; Lee, S.; Jun, S. C. Structural engineering and surface modification of MOF-derived cobalt-based hybrid nanosheets for flexible solid-state supercapacitors. *Energy Storage Mater.* **2020**, *32*, 167−177.

(2) Liu, S.; Kang, L.; Henzie, J.; Zhang, J.; Ha, J.; Amin, M. A.; Hossain, M. S. A.; Jun, S. C.; Yamauchi, Y. Recent Advances and Perspectives of Battery-Type Anode Materials for Potassium Ion Storage. *ACS Nano* **2021**, *15*, 18931−18973.

(3) Liu, S.; Kang, L.; Zhang, J.; Jun, S. C.; Yamauchi, Y. Carbonaceous Anode Materials for Non-aqueous Sodium- and Potassium-Ion Hybrid Capacitors. *ACS Energy Lett.* **2021**, *6*, 4127−4154.

(4) Chen, W. C.; Liu, Y. T.; Kuo, S. W. Mesoporous Organic/Inorganic Hybrid Materials with Frank-Kasper Phases Templated by an Unusual Linear Symmetry Diblock Copolymer. *Macromol. Rapid Commun.* **2021**, *42*, 2100302.

(5) Liu, S.; Kang, L.; Hu, J.; Jung, E.; Zhang, J.; Jun, S. C.; Yamauchi, Y. Unlocking the Potential of Oxygen-Deficient Copper-Doped Co3O4 Nanocrystals Confined in Carbon as an Advanced Electrode for Flexible Solid-State Supercapacitors. *ACS Energy Lett.* **2021**, *6*, 3011−3019.

(6) Xu, Z.; Sun, S.; Han, Y.; Wei, Z.; Cheng, Y.; Yin, S.; Cui, W. High-Energy-Density Asymmetric Supercapacitor Based on a Durable and Stable Manganese Molybdate Nanostructure Electrode for Energy Storage Systems. *Appl. Energy Mater.* **2020**, *3*, 5393−5404.

(7) Kuo, S. W. Hydrogen bonding mediated self-assembled structures from block copolymer mixtures to mesoporous materials. *Polym. Int.* **2022**, DOI: 10.1002/pi.6264.

(8) Young, C.; Park, T.; Yi, J. W.; Kim, J.; Hossain, M. S. A.; Kaneti, Y. V.; Yamauchi, Y. Advanced Functional Carbons and Their Hybrid Nanoarchitectures Towards Supercapacitor Applications. *ChemSusChem* **2018**, *11*, 3546−3558.

(9) Tan, Y.; Xu, C.; Chen, G.; Liu, Z.; Ma, M.; Xie, Q.; Zheng, N.; Yao, S. Synthesis of Ultrathin Nitrogen-Doped Graphitic Carbon Nanocages as Advanced Electrode Materials for Supercapacitor. *ACS Appl. Mater. Interfaces* **2013**, *5*, 2241−2248.

(10) Datta, K. K. R.; Balasubramanian, V. V.; Ariga, K.; Mori, T.; Vinu, A. Highly Crystalline and Conductive Nitrogen-Doped Mesoporous Carbon with Graphitic Walls and Its Electrochemical Performance. *Chem.—Eur. J.* **2011**, *17*, 3390−3397.

(11) Kim, J.; Kim, J. H.; Ariga, K. Redox-Active Polymers for Energy Storage Nanoarchitectonics. *Joule* **2017**, *1*, 739−768.

(12) Wang, Y.; Li, W.; Zhang, L.; Zhang, X.; Tan, B.; Hao, J.; Jian Zhang, J.; Wang, X.; Hu, Q.; Lu, X. Amorphous Cobalt Hydrogen Phosphate Nanosheets with Remarkable Electrochemical Performances as Advanced Electrode for Supercapacitors. *J. Power Sources* **2020**, *449*, 227487.

(13) Shi, R.; Han, C.; Duan, H.; Xu, L.; Zhou, D.; Li, H.; Li, J.; Kang, F.; Li, B.; Wang, G. Redox-Active Organic Sodium Anthraquinone-2-Sulfonate (AQS) Anchored on Reduced Graphene Oxide for High-Performance Supercapacitors. *Adv. Energy Mater.* **2018**, *8*, 1802088.

(14) Kim, D.; Kang, J.; Yan, B.; Seong, K.-d.; Piao, Y. Ambient Temperature Synthesis of Iron-Doped Porous Nickel Pyrophosphate Nanoparticles with Long-Term Chemical Stability for High-Performance Oxygen Evolution Reaction Catalysis and Supercapacitors. *ACS Sustainable Chem. Eng.* **2020**, *8*, 2843−2853.

(15) Wulan Septiani, N. L.; Kaneti, Y. V.; Fathoni, K. B.; Wang, J.; Ide, Y.; Yuliarto, B.; Nugraha, B.; Dipojono, H. K.; Nanjundan, A. K.; Golberg, D.; Bando, Y.; Yamauchi, Y. Self-Assembly of Nickel Phosphate-Based Nanotubes into Two-Dimensional Crumpled Sheet-Like Architectures for High-Performance Asymmetric Supercapacitors. *Nano Energy* **2020**, *67*, 104270.

(16) EL-Mahdy, A. F. M.; Yu, T. C.; Mohamed, M. G.; Kuo, S.-W. Secondary Structures of Polypeptide-Based Diblock Copolymers Influence the Microphase Separation of Templates for the Fabrication of Microporous Carbons. *Macromolecules* **2021**, *54*, 1030−1042.

(17) Eftekhari, A.; Fang, B. Electrochemical Hydrogen Storage: Opportunities for Fuel Storage, Batteries, Fuel Cells, and Supercapacitors. *Int. J. Hydrogen Energy* **2017**, *42*, 25143−25165.

(18) Mohamed, M. G.; Chen, T.-C.; Kuo, S.-W. Solid-State Chemical Transformations to Enhance Gas Capture in Benzoxazine-Linked Conjugated Microporous Polymers. *Macromolecules* **2021**, *54*, 5866−5877.

(19) Zhao, H.; Wang, J.; Zheng, Y.; Li, J.; Han, X.; He, G.; Du, Y. Organic Thiocarboxylate Electrodes for a Room-Temperature Sodium Ion Battery Delivering an Ultrahigh Capacity. *Angew. Chem., Int. Ed.* **2017**, *56*, 15334−15338.

(20) Mohamed, M. G.; Lee, C.-C.; EL-Mahdy, A. F. M.; Lüder, J.; Yu, M.-H.; Li, Z.; Zhu, Z.; Chueh, C.-C.; Kuo, S.-W. Exploitation of Two Dimensional Conjugated Covalent Organic Frameworks Based on Tetraphenylethylene with Bicarbazole and Pyrene Units and Applications in Perovskite Solar Cells. *J. Mater. Chem. A* **2020**, *8*, 11448−11459.

(21) Mohamed, M. G.; Mansoure, T. H.; Takashi, Y.; Mohamed Samy, M.; Chen, T.; Kuo, S.-W. Ultrastable porous organic/inorganic polymers based on polyhedral oligomeric silsesquioxane (POSS) hybrids exhibiting high performance for thermal property and energy storage. *Microporous Mesoporous Mater.* **2021**, *328*, 111505.

(22) Mohamed, M. G.; Chen, W.-C.; El-Mahdy, A. F. M.; Kuo, S.-W. Porous organic/inorganic polymers based on double-decker silsesquioxane for high-performance energy storage. *J. Polym. Res.* **2021**, *28*, 219.

(23) Mohamed, M. G.; Ahmed, M. M. M.; Du, W.-T.; Kuo, S.-W. Meso/Microporous Carbons from Conjugated Hyper-Crosslinked Polymers Based on Tetraphenylethene for High-Performance CO_2 Capture and Supercapacitor. *Molecules* **2021**, *26*, 738.

(24) Mohamed, M. G.; Atayde, E. C.; Matsagar, B. M.; Na, J.; Yamauchi, Y.; Wu, K. C.-W.; Kuo, S.-W. Construction Hierarchically Mesoporous/Microporous Materials Based on Block Copolymer and Covalent Organic Framework. *J. Taiwan Inst. Chem. Eng.* **2020**, *112*, 180−192.

(25) Gamal Mohamed, M.; Tsai, M.-Y.; Wang, C.-F.; Huang, C.-F.; Danko, M.; Dai, L.; Chen, T.; Kuo, S.-W. Multifunctional Polyhedral Oligomeric Silsesquioxane (POSS) Based Hybrid Porous Materials for CO_2 Uptake and Iodine Adsorption. *Polymers* **2021**, *13*, 221.

(26) Abuzeid, H. R.; EL-Mahdy, A. F. M.; Kuo, S.-W. Covalent organic frameworks: Design principles, synthetic strategies, and diverse applications. *Giant* **2021**, *6*, 100054.

(27) Mohamed, M. G.; EL-Mahdy, A. F. M.; Kotp, M. G.; Kuo, S.-W. Advances in Porous Organic Polymers: Syntheses, Structures, and Diverse Applications. *Mater. Adv.* **2022**, *3*, 707−733.

(28) Mohamed, M. G.; Zhang, X.; Mansoure, T. H.; El-Mahdy, A. F. M.; Huang, C.-F.; Danko, M.; Xin, Z.; Kuo, S.-W. Hypercrosslinked porous organic polymers based on tetraphenylanthraquinone for CO_2 uptake and high-performance supercapacitor. *Polymer* **2020**, *205*, 122857.

(29) EL-Mahdy, A. F. M.; Young, C.; Kim, J.; You, J.; Yamauchi, Y.; Kuo, S.-W. Hollow Microspherical and Microtubular [3+3] Carbazole-Based Covalent Organic Frameworks and Their Gas and Energy Storage Applications. *ACS Appl. Mater. Interface* **2019**, *11*, 9343−9354.

(30) Mohamed, M. G.; Sharma, S. U.; Yang, C.-H.; Samy, M. M.; Mohammed, A. A. K.; Chaganti, S. V.; Lee, J.-T.; Wei-Kuo, S. Anthraquinone-Enriched Conjugated Microporous Polymers as Organic Cathode Materials for High-Performance Lithium-Ion Batteries. *ACS Appl. Energy Mater.* **2021**, *4*, 14628−14639.

(31) Mohamed, M. G.; Liu, N. Y.; EL-Mahdy, A. F. M.; Kuo, S. W. Ultrastable Luminescent Hybrid Microporous Polymers Based on Polyhedral Oligomeric Silsesquioxane for CO_2 Uptake and Metal Ion Sensing. *Microporous Mesoporous Mater.* **2021**, *311*, 110695.

(32) Zhang, C.; He, Y.; Mu, P.; Wang, X.; He, Q.; Chen, Y.; Zeng, J.; Wang, F.; Xu, Y.; Jiang, J.-X. Toward High Performance Thiophene Containing Conjugated Microporous Polymer Anodes for Lithium-Ion Batteries through Structure Design. *Adv. Funct. Mater.* **2018**, *28*, 1705432.

(33) Fischer, S.; Schimanowitz, A.; Dawson, R.; Senkovska, I.; Kaskel, S.; Thomas, A. Cationic Microporous Polymer Networks by Polymerisation of Weakly Coordinating Cations with CO_2-Storage Ability. *J. Mater. Chem. A* **2014**, *2*, 11825−11829.

(34) Wang, H.; Cheng, Z.; Liao, Y.; Li, J.; Weber, J.; Thomas, A.; Faul, C. F. J. Conjugated Microporous Polycarbazole Networks as Precursors for Nitrogen-Enriched Microporous Carbons for CO_2 Storage and Electrochemical Capacitors. *Chem. Mater.* **2017**, *29*, 4885−4893.

(35) Liu, Y.-C.; Yeh, L.-H.; Zheng, M.-J.; Wu, K. C.-W. Highly selective and high-performance osmotic power generators in subnanochannel membranes enabled by metal-organic frameworks. *Sci. Adv.* **2021**, *7*, No. eabe9924.

(36) Bezzu, C. G.; Carta, M.; Tonkins, A.; Jansen, J. C.; Bernardo, P.; Bazzarelli, F.; Mckeown, N. B. A spirobifluorene-Based Polymer of Intrinsic Microporosity with Improved Performance for Gas Separation. *Adv. Mater.* **2012**, *24*, 5930−5933.

(37) Li, R.; Byun, J.; Huang, W.; Ayed, C.; Wang, L.; Zhang, K. A. I. Poly(benzothiadiazoles) and Their Derivatives as Heterogeneous Photocatalysts for Visible-Light-Driven Chemical Transformations. *ACS Catal.* **2018**, *8*, 4735−4750.

(38) Zhang, T.; Xing, G.; Chen, W.; Chen, L. Porous Organic Polymers: A Promising Platform for Efficient Photocatalysis. *Mater. Chem. Front.* **2020**, *4*, 332−353.

(39) Wang, B.; Xie, Z.; Li, Y.; Yang, Z.; Chen, L. Dual-Functional Conjugated Nanoporous Polymers for Efficient Organic Pollutants Treatment in Water: A Synergistic Strategy of Adsorption and Photocatalysis. *Macromolecules* **2018**, *51*, 3443−3449.

(40) Elewa, A. M.; EL-Mahdy, A. F. M.; Elsayed, M. H.; Mohamed, M. G.; Kuo, S.-W.; Chou, H.-H. Sulfur-doped triazine-conjugated microporous polymers for achieving the robust visible-light-driven hydrogen evolution. *Chem. Eng. J.* **2021**, *421*, 129825.

(41) Zhang, W.; Tang, J.; Yu, W.; Huang, Q.; Fu, Y.; Kuang, G.; Pan, C.; Yu, G. Visible Light-Driven C-3 Functionalization of Indoles over Conjugated Microporous Polymers. *ACS Catal.* **2018**, *8*, 8084−8091.

(42) Zhu, J.; Yang, C.; Lu, C.; Zhang, F.; Yuan, Z.; Zhuang, X. Two Dimensional Porous Polymers: From Sandwich-like Structure to Layered Skeleton. *Acc. Chem. Res.* **2018**, *51*, 3191−3202.

(43) EL-Mahdy, A. F. M.; Elewa, A. M.; Huang, S. W.; Chou, H. H.; Kuo, S. W. Dual-Function Fluorescent Covalent Organic Frameworks: HCl Sensing and Photocatalytic H_2 Evolution from Water. *Adv. Opt. Mater.* **2020**, *8*, 2000641.

(44) Hao, L.; Ning, J.; Luo, B.; Wang, B.; Zhang, Y.; Tang, Z.; Yang, J.; Thomas, A.; Zhi, L. Structural Evolution of 2D Microporous Covalent Triazine-Based Framework toward the Study of High-Performance Supercapacitors. *J. Am. Chem. Soc.* **2015**, *137*, 219−225.

(45) Zhuang, X.; Gehrig, D.; Forler, N.; Liang, H.; Wagner, M.; Hansen, M. R.; Laquai, F.; Zhang, F.; Feng, X. Conjugated microporous polymers with dimensionality-controlled heterostructures for green energy devices. *Adv. Mater.* **2015**, *27*, 3789−3796.

(46) Amin, K.; Ashraf, N.; Mao, L.; Faul, C. F. J.; Wei, Z. Conjugated microporous polymers for energy storage: Recent progress and challenges. *Nano Energy* **2021**, *85*, 105958.

(47) Li, Y.; Zheng, S.; Liu, X.; Li, P.; Sun, L.; Yang, R.; Wang, S.; Wu, Z. S.; Bao, X.; Deng, W. Q. Conductive Microporous Covalent Triazine-Based Framework for High-Performance Electrochemical Capacitive Energy Storage. *Angew. Chem., Int. Ed.* **2018**, *57*, 7992−7996.

(48) Feng, X.; Liang, Y.; Zhi, L.; Thomas, A.; Wu, D.; Lieberwirth, I.; Kolb, U.; Müllen, K. Synthesis of Microporous Carbon Nanofibers and Nanotubes from Conjugated Polymer Network and Evaluation in Electrochemical Capacitor. *Adv. Funct. Mater.* **2009**, *19*, 2125−2129.

(49) Samy, M. M.; Mohamed, M. G.; Mansoure, T. H.; Meng, T. S.; Khan, M. A. R.; Liaw, C.-C.; Kuo, S.-W. Solid state chemical transformations through ring-opening polymerization of ferrocene-based conjugated microporous polymers in host−guest complexes with benzoxazine-linked cyclodextrin. *J. Taiwan Inst. Chem. Eng.* **2022**, *132*, 104110.

(50) Zhang, K.; Hu, Y.; Wang, L.; Monteiro, M. J.; Jia, Z. Pyrene-Functionalized PTMA by NRC for Greater $\pi−\pi$ Stacking with rGO and Enhanced Electrochemical Properties. *ACS Appl. Mater. Interfaces* **2017**, *9*, 34900−34908.

(51) Han, Y.; Zhang, Q.; Hu, N.; Zhang, X.; Mai, Y.; Liu, J.; Hua, X.; Wei, H. Core-Shell Nanostructure of Single-Wall Carbon Nanotubes

and Covalent Organic Frameworks for Supercapacitors. *Chin. Chem. Lett.* **2017**, *28*, 2269−2273.

(52) Ran, F.; Yang, X.; Xu, X.; Bai, Y.; Shao, L. Boosting The Charge Storage of Layered Double Hydroxides Derived from Carbon Nanotube-Tailored Metal Organic Frameworks. *Electrochim. Acta* **2019**, *301*, 117−125.

(53) Zha, Z.; Xu, L.; Wang, Z.; Li, X.; Pan, Q.; Hu, P.; Lei, S. 3D Graphene Functionalized by Covalent Organic Framework Thin Film as Capacitive Electrode in Alkaline Media. *ACS Appl. Mater. Interfaces* **2015**, *7*, 17837−17843.

(54) Sengottaiyan, C.; Jayavel, R.; Shrestha, R. G.; Subramani, T.; Maji, S.; Kim, J. H.; Hill, J. P.; Ariga, K.; Shrestha, L. K. Indium Oxide/Carbon Nanotube/Reduced Graphene Oxide Ternary Nanocomposite with Enhanced Electrochemical Supercapacitance. *Bull. Chem. Soc. Jpn.* **2019**, *92*, 521−528.

(55) Li, J.; Lu, W.; Yan, Y.; Chou, T.-W. High Performance Solid-State Flexible Supercapacitor Based on Fe$_3$O$_4$/Carbon Nanotube/Polyaniline Ternary Films. *J. Mater. Chem. A* **2017**, *5*, 11271−11277.

(56) Samy, M. M.; Mohamed, M. G.; Kuo, S.-W. Pyrene Functionalized Tetraphenylethylene Polybenzoxazine for Dispersing Single-Walled Carbon Nanotubes and Energy Storage. *Compos. Sci. Technol.* **2020**, *199*, 108360.

(57) Mei, L.; Cui, X.; Duan, Q.; Li, Y.; Lv, X.; Wang, H.-g. Metal Phthalocyanine-Linked Conjugated Microporous Polymer Hybridized with Carbon Nanotubes as a High-Performance Flexible Electrode for Supercapacitors. *Int. J. Hydrogen Energy* **2020**, *45*, 22950−22958.

(58) Zhang, Y.; Lin, B.; Sun, Y.; Zhang, X.; Yang, H.; Wang, J. Carbon Nanotubes@Metal-Organic Frameworks as Mn-Based Symmetrical Supercapacitor Electrodes for Enhanced Charge Storage. *RSC Adv.* **2015**, *5*, 58100−58106.

(59) Samy, M. M.; Mohamed, M. G.; EL-Mahdy, A. F. M.; Mansoure, T. H.; Wu, K. C.-W.; Kuo, S.-W. High performance supercapacitor electrodes prepared from dispersions of tetrabenzonaphthalene-based conjugated microporous polymers and carbon nanotubes. *ACS Appl. Mater. Interfaces* **2021**, *13*, 51906−51916.

(60) Wołek, B.; Werłos, M.; Komander, M.; Kudelko, A. Efficient Synthesis of Novel 1,3,4-Oxadiazoles Bearing a 4-N,N-Dimethylaminoquinazoline Scaffold via Palladium-Catalyzed Suzuki Cross-Coupling Reactions. *Molecules* **2020**, *25*, 5150.

(61) Tang, L.; Zheng, Z.; Huang, Z.; Zhong, K.; Bian, Y.; Nandhakumar, R. Multi-analyte, ratiometric and relay recognition of a 2,5-diphenyl-1,3,4-oxadiazole-based fluorescent sensor through modulating ESIPT. *RSC Adv.* **2015**, *5*, 10505−10511.

(62) Paun, A.; Hadade, N. D.; Paraschivescu, C. C.; Matache, M. 1,3,4-Oxadiazoles as luminescent materials for organic light emitting diodes via cross-coupling reactions. *J. Mater. Chem. C* **2016**, *4*, 8596−8610.

(63) Dai, C.; Zhong, L.; Gong, X.; Zeng, L.; Xue, C.; Li, S.; Liu, B. Triphenylamine based conjugated microporous polymers for selective photoreduction of CO$_2$ to CO under visible light. *Green Chem.* **2019**, *21*, 6606−6610.

(64) Yang, X.; Duan, L.; Ran, X.; Yi, S. Conjugated microporous polymer bearing 1,3,4-oxadiazole and thienyl moieties for decomposition of organic dyes under visible light. *React. Funct. Polym.* **2021**, *168*, 105051.

(65) Mohamed, M. G.; Elsayed, M. H.; Elewa, A. M.; EL-Mahdy, A. F. M.; Yang, C.-H.; Mohammed, A. A. K.; Chou, H.-H.; Kuo, S.-W. Pyrene Containing Conjugated Organic Microporous Polymers for Photocatalytic Hydrogen Evolution from Water. *Catal. Sci. Technol.* **2021**, *11*, 2229−2241.

(66) Mohamed, M. G.; Kuo, S. W. Functional Silica and Carbon Nanocomposites Based on Polybenzoxazines. *Macromol. Chem. Phys.* **2019**, *220*, 1800306.

(67) Zhang, C.; Xiao, P.; Ni, F.; Gu, J.; Chen, J.; Nie, Y.; Kuo, S.-W.; Chen, T. Breathable and superhydrophobic photothermic fabric enables efficient interface energy management via confined heating strategy for sustainable seawater evaporation. *Chem. Eng. J.* **2022**, *428*, 131142.

(68) Zindy, N.; Aumaitre, C.; Mainville, M.; Saneifar, H.; Johnson, P. A.; Bélanger, D.; Leclerc, M. Pyrene Diimide Based π-Conjugated Copolymer and Single-Walled Carbon Nanotube Composites for Lithium-Ion Batteries. *Chem. Mater.* **2019**, *31*, 8764−8773.

(69) Mei, L.; Wei, J.-C.; Duan, Q. Construction of copper porphyrin-linked conjugated microporous polymer/carbon nanotube composite as flexible electrodes for supercapacitors. *J. Mater. Sci. Mater. Electron.* **2021**, *32*, 24953−24963.

(70) Mohamed, M. G.; Samy, M. M.; Mansoure, T. H.; Li, C.-J.; Li, W.-C.; Chen, J.-H.; Zhang, K.; Kuo, S.-W. Microporous Carbon and Carbon/Metal Composite Materials Derived from Bio-Benzoxazine-Linked Precursor for CO$_2$ Capture and Energy Storage Applications. *Int. J. Mol. Sci.* **2022**, *23*, 347.